Tunable Superlattice p–i–n Photodetectors: Characteristics, Theory, and Applications

ANDERS LARSSON, PETER A. ANDREKSON, STUDENT MEMBER, IEEE, SVERRE T. ENG, MEMBER, IEEE, AND AMNON YARIV, FELLOW, IEEE

Abstract—**We report on extended measurements and theory on the recently developed monolithic wavelength demultiplexer consisting of voltage tunable superlattice p–i–n photodetectors in a waveguide configuration. This includes a reduced wavelength spacing, an investigation of the polarization dependence of the crosstalk and bit-error-rate measurements for various crosstalk levels. We show that the device is able to demultiplex and detect two optical signals with a wavelength separation of 20 nm directly into different electrical channels at a data rate of 1 Gbit/s and with a crosstalk attenuation varying between 20 and 28 dB, depending on the polarization. The minimum acceptable crosstalk attenuation at a data rate of 100 Mbits/s is determined to be 10 dB. The feasibility of using the device as a polarization angle sensor for linearly polarized light is also demonstrated. The paper includes a theory for the emission of photogenerated carriers out of the quantum wells since this is potentially a speed limiting mechanism in these detectors. We show that a theory of thermally assisted tunneling by polar optical phonon interaction is able to predict emission times consistent with the observed temporal response.**

I. Introduction

RECENT developments in epitaxial growth techniques with monolayer precision such as molecular beam epitaxy (MBE) [1] and metal-organic chemical vapor deposition (MOCVD) [2] have made possible a new class of optoelectronic devices based on physical phenomena in quantum wells and superlattices [3]. In these materials the carriers are confined to thin semiconductor layers. When the layer thickness approaches the Bohr radius, the electronic system enters the quantum regime and the material exhibits modified electrical and optical properties as compared to bulk material [4]. Among these so-called quantum size effects are the step-like density of states function [5], the structure dependent energy spectrum of allowed states [6], the room temperature excitonic nonlinear [7] and polarization dependent [8] absorption, and the enhanced electroabsorption effect [9]. New and improved optoelectronic devices such as quantum well lasers [10], nonlinear optical elements [11], infrared detectors [12], [13] and electroabsorption devices for optical modulation and detection have been fabricated using these materials.

The enhanced electroabsorption effect in quantum well structures with the electric field applied perpendicular to the plane of the layers originates from a field induced lowering of the ground state energies in the quantum wells [14]. This will shift the band edge to lower photon energies while still retaining the excitonic resonances and consequently a sharp band edge. This effect, known as the quantum confined Stark effect (QCSE) [9], [15], [16], has recently been investigated for high-speed optical modulators [17], [18], self-electrooptic effect devices [19], actively Q-switched quantum well lasers [20], size effect modulation light sources [21], and voltage tunable photodetectors [22], [23]. The latter device is realized by incorporating a superlattice or a multiple quantum well structure in the undoped depletion region of a p–i–n doped detector. When the reverse bias voltage is increased, the electric field increases in the quantum wells and consequently the absorption edge moves to longer wavelengths as predicted by the QCSE. In some recent publications we have briefly demonstrated the feasibility of high-speed detection [23] and monolithic wavelength demultiplexing [24] using such superlattice p–i–n photodetectors (SLPD).

In this paper we present results from extended measurements on the performance of the monolithic wavelength demultiplexer including a reduced wavelength spacing, a polarization-dependent crosstalk, and bit-error-rate degradation due to crosstalk as well as application to polarization sensitive detection. We also present a theory for the emission of photogenerated carriers out of the quantum wells since this is potentially a speed limiting mechanism in SLPD's. We show that a theory of thermally assisted tunneling by polar optical phonon interaction is able to predict emission times consistent with the observed temporal response.

The paper is organized as follows. In Section II we describe the device structure and fabrication. In Section III the characteristics of an individual SLPD are described in detail. This includes the spectral characteristics (Section III-A), the responsivity (Section III-B), and the high-frequency characteristics (Section III-C). In Section IV a theory of thermally assisted tunneling is presented. The performance of the device as a monolithic wavelength demultiplexer is described in Section V. In Section VI we show that the same device can be used to determine the

Manuscript received August 18, 1987. This work was supported by the National Swedish Board for Technical Development and by the Office of Naval Research, the ITT Corporation, and NASA/JPL.

A. Larsson and P. A. Andrekson are with the Department of Electrical Measurements, Chalmers University of Technology, Göteborg, Sweden.

S. T. Eng is with the Department of Electrical Measurements, Chalmers University of Technology, Göteborg, Sweden, and the Jet Propulsion Laboratory, California Institute of Technology, Pasadena, CA 91109.

A. Yariv is with the Department of Applied Physics, California Institute of Technology, Pasadena, CA 91125.

IEEE Log Number 8820039.

0018-9197/88/0500-0787$01.00 © 1988 IEEE

polarization angle of linearly polarized light. The concluding section, Section VII, summarizes our results.

II. Device Structure and Fabrication

The device structure is shown schematically in Fig. 1. The epitaxial layers were grown by molecular beam epitaxy (MBE) in a RIBER 2300 R&D system with continuous substrate rotation and using solid sources. The substrate temperature was kept at 630°C throughout the growth. The following layers were sequentially grown on an n^+-GaAs substrate: a 1.0 μm thick n^+-GaAs buffer layer ($4 \cdot 10^{18}$ cm^{-3}), a 1.0 μm thick n-$Al_{0.25}Ga_{0.75}As$ layer ($5 \cdot 10^{17}$ cm^{-3}), a 385 Å thick undoped superlattice buffer, a 1.0 μm thick undoped $GaAs/Al_{0.25}Ga_{0.75}As$ (100/50 Å) superlattice, a 385 Å thick undoped superlattice buffer, a 1.0 μm thick p-$Al_{0.25}Ga_{0.75}As$ layer ($5 \cdot 10^{17}$ cm^{-3}), and finally a 0.2 μm thick p^+-GaAs contact layer ($1 \cdot 10^{19}$ cm^{-3}). The superlattice buffers have seven 20 Å thick GaAs layers and six $Al_{0.25}Ga_{0.75}As$ layers with a thickness graded from 50 to 20 Å towards the superlattice. Introduction of a superlattice buffer has been shown to reduce the unintentional doping level in the succeeding layers due to impurity trapping at the buffer layer interfaces [25], [26]. As will be shown in Section III-A, a low doping level in the superlattice is important for the wavelength selectivity of the SLPD. The second superlattice buffer was introduced for symmetry purposes.

After epitaxial growth, separate SLPD's were defined using proton implantation (120 keV, $5 \cdot 10^{14}$ cm^{-2}). The proton energy was adjusted to produce an implantation depth equal to the total thickness of the p-doped layers. This provides electrical isolation between the detectors (>1 GΩ) and reduces the capacitance of the individual diodes to about 0.7 pF. After metallization and lapping, the chip was cleaved into individual two-element edge detectors and mounted for high-speed operation. The final capacitance of each diode, including the submount capacitance, was about 0.9 pF at the operating bias voltage. In Fig. 2 we show a typical current–voltage characteristic of a mounted and bonded detector. The reverse breakdown voltage is 38 V which corresponds to an average electric field of about 400 kV/cm. This is similar to the maximum field at avalanche breakdown for one-sided abrupt junctions in GaAs for the same doping level [27]. The dark current was less than 1 nA at the maximum operating bias voltage of -15 V.

This detector geometry facilitates the fabrication of small area, low capacitance photodetectors suitable for high-speed operation. However, due to the small detector area seen by the incident optical signal, a precise alignment of the focusing lens (and/or optical fiber) and the detector is required for efficient coupling. The structure also provides waveguiding perpendicular to the plane of the layers, and is therefore compatible with integrated optoelectronics. The device essentially consists of two monolithically integrated and electrically isolated SLPD's in a waveguide configuration. By applying different reverse bias voltages to the two detectors and thereby tuning

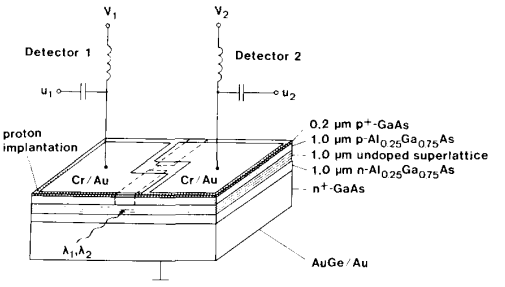

Fig. 1. Schematic view of the dual-wavelength demultiplexing superlattice p-i-n waveguide detector array. The detectors are 20 μm wide, the lengths of detectors 1 and 2 are 20 and 50 μm, respectively, and the separation is 10 μm.

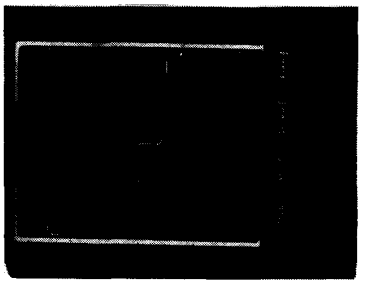

(a)

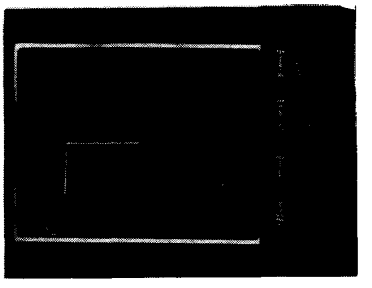

(b)

Fig. 2. I–V characteristics of a superlattice p-i-n detector. (a) Forward bias. (b) Reverse bias.

the absorption edges to different wavelengths, the device will act as a dual wavelength demultiplexer for two appropriately chosen wavelengths.

III. Characteristics of Individual Detectors

A. Spectral Characteristics

The spectral characteristics of a SLPD were studied by illuminating the detector with light from an unpolarized monochromatic light source with a spectral resolution of about 3 nm. The photocurrent was measured as a function of wavelength for different applied reverse bias voltages. All measurements were made at room temperature. Representative photocurrent spectra at the band edge are

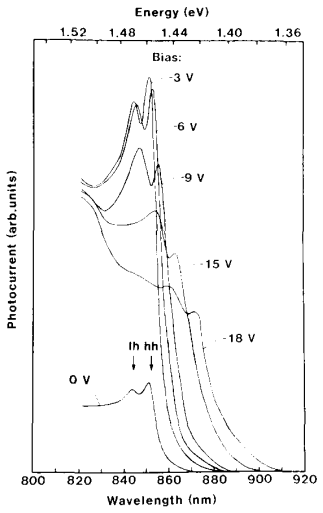

Fig. 3. Photocurrent spectra measured under different applied reverse bias voltages. The arrows indicate the calculated heavy hole (*hh*) and light hole (*lh*) excitonic transition energies without an external applied field.

shown in Fig. 3. The main features of these spectra are the clearly resolved excitonic resonances and the pronounced redshift with increasing reverse bias voltage.

The room temperature excitonic resonances are a consequence of the carrier confinement in the quantum wells which increases the binding energy of the excitons above that for bulk material [28]. The two excitonic peaks at the band edge correspond to the first quantized heavy hole-to-electron and light hole-to-electron excitons. Also shown in the figure (by arrows) are the calculated spectral positions of these excitonic resonances under zero field conditions as given by

$$E_{ex} = E_g + E_{e1} + E_{h1} - E_b \tag{1}$$

where E_g is the GaAs bandgap, E_{e1} and E_{h1} are the electron and (heavy or light) hole ground state energy levels in the quantum well, respectively, and E_b is the excitonic binding energy. The quantized energy levels (or subband energies) E_s can be found by solving the eigenvalue equations

$$\tan\sqrt{\frac{m_w^* E_s L_w^2}{2\hbar^2}} = \sqrt{\frac{m_B^*(V_B - E_s)}{m_w^* E_s}} \tag{2}$$

$$\cot\sqrt{\frac{m_w^* E_s L_w^2}{2\hbar^2}} = -\sqrt{\frac{m_B^*(V_B - E_s)}{m_w^* E_s}}. \tag{3}$$

Here L_w is the quantum well width, m_w^* and m_B^* are the carrier effective masses in the quantum well and the barrier, respectively, and V_B is the potential barrier height. The latter depends on the band offsets. In this and the following calculations we assume a ratio between the conduction and valence band offsets of 57/43 percent according to Miller *et al.* [29]. The parameters used in the calculations are summarized in Table I. The excitonic binding energies in the quantum wells (L_w = 100 Å, x = 0.25) were estimated as 8 and 9 meV for the heavy hole and the light hole exciton, respectively, [30]. As seen in Fig. 3 we obtain a good agreement between the calculated and the measured spectral positions of the excitonic transitions.

TABLE I
$Al_xGa_{1-x}As$ Band Parameters at Room Temperature Used in the Calculations

Bandgap:	$E_{g_{Al_xGa_{1-x}As}} = 1.424 + 1.247 \cdot x$ [eV]
Effective masses:	$m^*_{e_{Al_xGa_{1-x}As}} = (0.0665 + 0.0835 \cdot x) \cdot m_o$
	$m^*_{hh_{Al_xGa_{1-x}As}} = (0.34 + 0.42 \cdot x) \cdot m_o$
	$m^*_{lh_{Al_xGa_{1-x}As}} = (0.094 + 0.043 \cdot x) \cdot m_o$
Band offsets:	Q_c = 57 percent
	Q_v = 43 percent
Static dielectric constant:	$\epsilon_s = (13.18 - 3.12 \cdot x) \cdot \epsilon_o$
High-frequency dielectric constant:	$\epsilon_\infty = (10.89 - 2.73 \cdot x) \cdot \epsilon_o$

The low responsivity observed for the 0 V spectra is due to an incomplete depletion of the undoped region and consequently a reduced internal quantum efficiency. The bias required for full depletion was determined from capacitance versus voltage measurements to be −2 V. These data can be used to estimate the background doping level in the superlattice, using the expression for the depletion width for a one-sided abrupt junction [31]

$$W = \sqrt{\frac{2\epsilon_s}{eN_A}\left(V_{bi} - V_b - \frac{2kT}{e}\right)} \tag{4}$$

where ϵ_s is the static dielectric constant (Table I), V_{bi} is the built-in voltage, V_b is the applied reverse bias voltage, and N_A is the impurity concentration in the superlattice which is assumed to be p-type due to unintentional incorporation of carbon during the MBE-growth [32]. By using an average static dielectric constant for the superlattice, we obtain a doping level of $5 \cdot 10^{15}$ cm^{-3}. When the reverse bias voltage exceeds 2 V, the electric field distribution in the superlattice can be found by solving the Poisson equation assuming that the superlattice is fully depleted and taking charge neutrality into account. The result from such a calculation is shown in Fig. 4. Here we notice a nonuniform field distribution through the 1 μm thick superlattice due to the relatively high impurity concentration.

The electric field dependence of the excitonic resonances can be explained by the QCSE [9], [15], [16]. When the reverse bias voltage, and consequently the electric field perpendicular to the superlattice layers is increased, the excitonic resonances are shifted to lower energies. The dominant contribution to this shift is a field induced lowering of the ground state energy levels in the quantum wells. This effect can be approximately described through perturbational calculations [14] (valid in the low-field region), where the energy shift due to an applied electric field F of the ground state energy level in a quantum well of width L_w and with infinite barrier

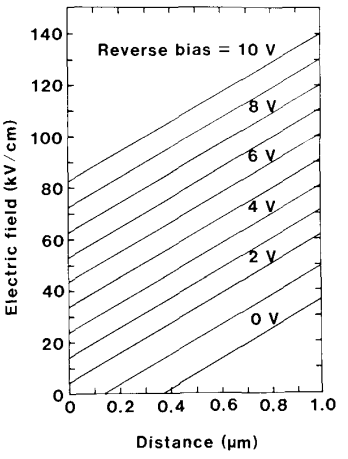

Fig. 4. Calculated electric field distribution through the superlattice under different applied reverse bias voltages.

heights is given by

$$\Delta E = \frac{m^* e^2 F^2 L_w^4}{24\hbar^2} \frac{1}{\pi^2} \left(1 - \frac{15}{\pi^2}\right). \tag{5}$$

The shift is thus proportional to the square of the electric field and to the carrier effective mass, and consequently the heavy hole exciton is shifted more than the light hole exciton for a certain applied field. For high fields the shift is almost linear [15]. An exact numerical solution of the Schrödinger equation for an isolated quantum well of finite depth, subjected to an electric field, can be obtained as linear combinations of Airy functions [33]. This field induced shift of the energy levels is counteracted by a reduction in the exciton binding energy due to the field induced polarization of the electron and hole wavefunctions [34]. This is, however, one order of magnitude smaller than the field induced ground state lowering, and tends to saturate at higher fields. The net effect is a marked redshift of the excitonic resonances. Even at high electric fields the exciton is strongly bound, compared to the bulk exciton, due to the confinement and the excitonic resonance remains resolvable at electric field exceeding 200 kV/cm [35].

As the applied electric field is increased, the oscillator strength of the excitonic resonances is also reduced. This is mainly a consequence of the reduced overlap integral between the polarized electron and hole wavefunctions perpendicular to the plane of the layers [16]. An important aspect for the wavelength selectivity of a device based on this electroabsorption effect is the broadening of the excitonic resonances with increasing reverse bias. Under zero-field conditions, the width of the exciton peak originates from interactions with thermal phonons [36]. This is the main broadening mechanism at room temperature. There is also a contribution from variations in the well thickness of the order of one monolayer along the plane of the layers [37]. When an electric field is applied, these broadening mechanisms become more efficient due to the reduced excitonic binding energy and the exciton width increases slightly [38]. At high fields ($>10^5$ V/cm), additional broadening is produced by field induced tunneling of the carriers out of the quantum wells [39]. In the present SLPD, however, the main broadening mechanism is the difference in excitonic transition energies through the superlattice caused by the field inhomogeneity. It is therefore of major importance to reduce the background doping level to obtain a high wavelength selectivity at the band edge.

Our measurement of the photocurrent spectra (using unpolarized light) gives no information on the polarization sensitivity of the detector. It has been shown, however, that the absorption in quantum well waveguides is highly anisotropic [8]. This is a result of quantum mechanical selection rules that govern the optically induced transitions [40]. For incident polarization parallel to the plane of the layers, both heavy hole and light hole excitons are observed. When the incident polarization is perpendicular to the plane of the layers, the heavy hole exciton peak disappears and its strength is transferred to the remaining light hole exciton. This anisotropy is preserved in the presence of large applied electric fields [35]. As we will see later, this causes a polarization dependence of the crosstalk in the wavelength demultiplexer (Section V) and can also be used to operate the device as a polarization angle sensor for linearly polarized light (Section VI).

B. Responsivity

The responsivities for the individual SLPD's were measured under conditions similar to those used in the demultiplexing experiment, with the excitation wavelengths resonant with the heavy hole excitons (Fig. 12, Section V). The two detectors were biased at -5 and -15 V, respectively. Two semiconductor lasers continuously operating at 850 and 870 nm, respectively, with the light polarized parallel to the plane of the superlattice layers (TE-polarized) were used. The outputs of the lasers were focused onto the cleaved edge of the detector using two microscope objectives. The responsivities for detectors 1 and 2 were measured to be 0.20 and 0.12 A/W, corresponding to external quantum efficiencies of 30 and 17 percent, respectively.

The measured responsivities can be analyzed by using a general expression for the external quantum efficiency of a waveguide detector, neglecting surface recombination effects [41]

$$\eta_{\text{ext}} = \kappa(1 - R) \frac{\Gamma\alpha_{ib}}{\alpha} (1 - e^{-\alpha L}) \eta_{\text{int}} \tag{6}$$

κ is the coupling efficiency, which accounts for the difference between the intensity profiles of the incident light and the waveguide mode. R is the reflection coefficient at the cleaved edge, Γ is the optical confinement factor, L is the length of the detector, α_{ib} is the interband absorption at the excitation wavelength, and α is the loss coefficient of the propagating optical mode given by

$$\alpha = \Gamma\alpha_{ib} + \Gamma\alpha_{fc} + (1 - \Gamma)\alpha_{fcx} + \alpha_s \tag{7}$$

where α_{fc} and α_{fcx} is the free carrier absorption in the superlattice and in the cladding layers (n- and p-AlGaAs), respectively. These latter parameters can be neglected for the doping levels used in the SLPD. The scattering loss in the waveguide, α_s, includes lateral spreading of the optical beam propagating along the waveguide due to the absence of any guiding mechanism parallel to the layers. From the saturation behavior of the responsivity when the reverse bias voltage exceeds 2 V, we conclude that the internal quantum efficiency η_{int}, i.e., the probability that a photogenerated electron–hole pair will be collected in the external contacts, approaches 100 percent at the operating bias voltage. The corresponding responsivity is given by

$$R = \frac{e}{h\nu}\eta_{\text{ext}} \tag{8}$$

where $h\nu$ is the photon energy.

The weak absorption close to the band edge in bulk material is in the SLPD compensated for by the excitonic resonances. Absorption coefficients $> 10^4\ \text{cm}^{-1}$ have been measured at the heavy hole exciton [42]. Also the longer interaction length in the waveguide detector compared to conventional photodiodes increases the effective absorption. The main losses in the first detector are therefore due to reflection at the cleaved edge, coupling loss resulting from the difference between the intensity profiles of the incident light and the waveguide mode and lateral spreading of the propagating mode. The second detector suffers from additional loss due to crosstalk into the first detector, loss in the region between the detectors, and additional spreading in the plane of the layers. A substantial improvement in responsivities could be achieved by antireflection coating the cleaved edge, by introducing waveguiding parallel to the layers, and by using mode matching optics.

C. High-Frequency Characteristics

The high-frequency response of a p–i–n photodiode depends on both the circuit bandwidth and on the drift velocity of photogenerated carriers through the depletion region [43]. Speed limitations due to diffusion of carriers generated by absorption outside the fully depleted undoped region (under operating conditions) is eliminated in the SLPD by the use of wide bandgap AlGaAs in the p- and n-regions. The fact that the carriers in a SLPD are transported through the superlattice layers, perpendicular to the potential barriers, under an applied electric field, naturally raises the question whether this might reduce the effective drift velocity through carrier trapping effects at the interfaces. An understanding of this perpendicular transport phenomenon is therefore of great importance for the design of SLPD's. Before discussing the transport mechanism we present results from temporal response measurements and consider bandwidth limitations due to parasitic circuit elements.

The detectors were excited with short optical pulses,

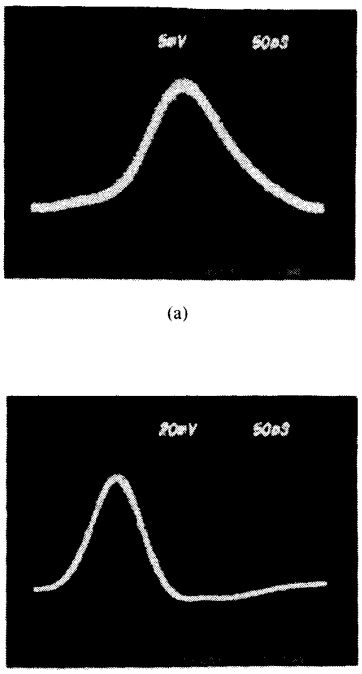

(a)

(b)

Fig. 5. Measured pulse response using short semiconductor laser pulses. (a) Detector 1, bias = −5 V, wavelength = 850 nm. (b) Detector 2, bias = −15 V, wavelength = 870 nm.

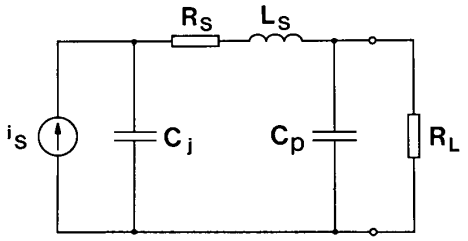

Fig. 6. Equivalent circuit for the detector including bonding wire inductance L_s, submount capacitance C_p, diode series resistance R_s, junction capacitance C_j, and a photocurrent source i_s.

~ 80 ps full width at half maximum (FWHM) from semiconductor lasers, incident on the cleaved edge of the device. The excitation wavelengths were resonant with the heavy hole exciton. Fig. 5 shows the results of the measurements. At a bias of −15 V [Fig. 5(b)] the pulse response FWHM is 95 ps. This is well explained by considering the combined effect of the optical pulse FWHM and the detector circuit bandwidth. In Fig. 6 we show an equivalent circuit for the mounted and bonded detector. This includes a current source i_s representing the current induced by the photogenerated carriers drifting through the undoped region, the junction capacitance C_j (0.7 pF at the operating bias voltage), the series resistance R_s (3 Ω), the bonding wire inductance L_s (1 nH), the submount capacitance C_p (0.2 pF), and the load resistance R_L (50 Ω). The 3 dB bandwidth of this circuit is 6.1 GHz. It

should be noted that the proper inclusion of the bonding wire inductance increases the bandwidth by as much as 2.7 GHz. If we assume an 80 ps FWHM Gaussian current pulse, produced by the incident optical pulse, we obtain an output pulse with a FWHM of about 90 ps after being filtered through the equivalent circuit. This is in good agreement with the observed response of 95 ps FWHM, taking the risetime of the sampling head into account. We therefore conclude that any bandwidth limiting effect due to a reduced effective drift velocity was not observed under this bias condition. At a bias voltage of -5 V [Fig. 5(a)], however, the response is not limited by the optical pulse FWHM or the circuit bandwidth. The observed response is asymmetric with a slower trailing edge and a FWHM of 150 ps. As we have reported earlier [23], the pulse response FWHM continuously increases with further decreased bias voltage, and is in the ns-range at 0 V bias. We believe that this is a result of an electric field dependent effective drift velocity perpendicular to the superlattice layers.

IV. Theory of Phonon Assisted Tunneling

The dominant perpendicular transport mechanism in a superlattice is strongly dependent on the prevailing conditions [44]. In the low field limit, transport proceeds by miniband conduction if the mean free path of the carriers appreciately exceeds the superlattice period [45]. In our particular device, however, the energy drop across a superlattice period, due to the applied electric field (average fields larger than 50 kV/cm), exceeds the miniband width and the miniband breaks up in a ladder of localized quasi-bound states [46]. The states of the superlattice are no longer Bloch waves, but are localized in the wells along the direction perpendicular to the layers. Also effects such as intralayer and interlayer fluctuations, alloy disorder, and the unavoidable presence of phonon scattering tend to disturb the coherence of the wavefunction and the formation of extended Bloch states. In this case the conduction may proceed by phonon-assisted tunneling between adjacent layers (hopping conduction) [47]. Both calculations [48] and conductivity measurements [49] have, however, confirmed the very low mobility for this transport mechanism inconsistent with the fast temporal response of the SLPD. We therefore believe that the photogenerated carriers are emitted out of the quantum wells to the continuum of states above the potential barriers and subsequently travel a mean free path before being recaptured by one of the wells. The mean free path may be several superlattice periods due to the reduced carrier thermalization in two-dimensional systems [50] and the large energy gained by the carriers between collisions.

Next we show that the time constants for such an emission process can satisfactorily explain the observed temporal response of the SLPD. We present a theory for thermally assisted tunneling of carriers out of the quantum wells at high electric fields (>50 kV/cm). The thermal interaction with the lattice is accounted for by polar optical phonon scattering, which is the dominant scattering mechanism in polar semiconductors such as GaAs at room temperature [51]. Recently reported experiments on the temperature-dependent characteristics of similar structures support a phonon assisted transport mechanism [52], [53].

We start the analysis by considering the electric field dependent tunneling of confined carriers through the potential structure. The model potential used in the tunneling calculations is shown in Fig. 7. We consider a quasi-bound carrier in energy level number s with the corresponding energy E_s associated with the quantization perpendicular to the superlattice layers. E_s is calculated using (2) and (3). The electric field induced change of the energy levels was found to have a negligible effect on the tunneling probabilities and is therefore neglected in the theory presented here. The band parameters used in the calculations are summarized in Table I. We approximate the carrier wavevector perpendicular to the layers with that valid for infinite potential barriers

$$k = s\frac{\pi}{L_w}. \tag{9}$$

The carrier confined in the well can be regarded as oscillating back and forth with a corresponding velocity $\hbar k/m^*$ and therefore colliding with one of the barriers with a collision frequency

$$f = s\frac{\hbar\pi}{2L_w^2 m^*}. \tag{10}$$

Each time the carrier strikes the right barrier it has a certain probability T_p for tunneling through the potential structure. The escape probability per unit time is then given by

$$P = fT_p. \tag{11}$$

Finally, we can define a tunneling lifetime as the inverse of the escape probability per unit time

$$\tau = \frac{1}{T_p}\frac{2L_w^2 m^*}{\hbar\pi s}. \tag{12}$$

The tunneling probability is evaluated using the transfer matrix technique in the effective mass approximation [54]. As a model potential we use the square potential profile, indicated by the dashed line in Fig. 7. This simplifies the calculations considerably through the use of plane wave functions for the carrier in each region m. We consider tunneling from region 1 to region n as illustrated in the figure with the corresponding carrier wavefunctions

$$\Psi_1 = e^{ik_1 z} + Re^{-ik_1 z} \tag{13}$$

$$\Psi_n = Te^{ik_n z} \tag{14}$$

where R and T are the reflection and transmission amplitudes, respectively. Ψ_1 describes the incident and reflected wave at the right barrier in region 1. Ψ_n is the transmitted carrier wavefunction in region n. The transmission through the structure is then described by a ($2\times$

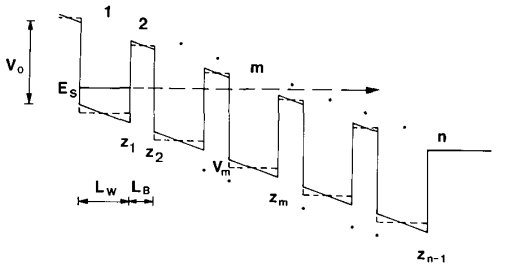

Fig. 7. Model potential used in the tunneling lifetime calculations.

2)-matrix which is the product of matrices obtained by matching the wavefunctions and their derivatives divided by the effective masses [55] at each of the $n-1$ interfaces

$$\begin{bmatrix} T \\ 0 \end{bmatrix} = \begin{bmatrix} M_{11} & M_{12} \\ M_{21} & M_{22} \end{bmatrix} \begin{bmatrix} 1 \\ R \end{bmatrix} \tag{15}$$

where

$$\begin{bmatrix} M_{11} & M_{12} \\ M_{21} & M_{22} \end{bmatrix} = \prod_{m=1}^{n-1} \begin{bmatrix} \frac{1}{2}\left(1 + \frac{m^*_{m+1}k_m}{m^*_m k_{m+1}}\right) e^{i(k_m - k_{m+1})z_m} & \frac{1}{2}\left(1 - \frac{m^*_{m+1}k_m}{m^*_m k_{m+1}}\right) e^{-i(k_m + k_{m+1})z_m} \\ \frac{1}{2}\left(1 - \frac{m^*_{m+1}k_m}{m^*_m k_{m+1}}\right) e^{i(k_m + k_{m+1})z_m} & \frac{1}{2}\left(1 + \frac{m^*_{m+1}k_m}{m^*_m k_{m+1}}\right) e^{-i(k_m - k_{m+1})z_m} \end{bmatrix} \tag{16}$$

and

$$k_m = \sqrt{\frac{2m^*_m(E_s - V_m)}{\hbar^2}}. \tag{17}$$

V_m is the potential (which is a function of the applied electric field) and m^*_m is the carrier effective mass in region m. The amplitude of the transmitted wave is then given by

$$T = M_{11} - \frac{M_{12}M_{21}}{M_{22}}. \tag{18}$$

Finally, the transmission probability is calculated as

$$T_p = TT^*. \tag{19}$$

Using this expression combined with (12), the tunneling lifetimes as a function of applied electric field can be calculated. Results from these calculations are shown in Fig. 8(a)–(c). Here we show the tunneling lifetimes from all the quasi-bound states in the quantum well except for the heavy holes where we have omitted $s = 2$ and $s = 4$ for clarity. The number of barriers taken into account is 20. From these results the following conclusions can be made. 1) The tunneling lifetime initially decreases rapidly with increasing electric field. This is due to the fact that the tunneling lifetime is a strong function of the number of barriers the carrier has to penetrate. When the electric field is increased this number drops rapidly and at the field strength used in the SLPD (>50 kV/cm) only one barrier has to be penetrated. 2) The inclusion of barriers which the carriers cross mainly introduces fine structure in the tunneling lifetime versus electric field. The result is thus not very sensitive to the number of barriers used in the calculations as long as the penetrated barriers are included. This was verified by varying the total number of barriers in the calculations. 3) At the operating bias voltage of the SLPD the electron and light hole tunneling lifetimes from the ground states are on the order of 10–100 ps while that of the heavy holes are 10 ns. 4) For the highest quasi-bound states for each carrier in the well ($s = 2$ for the electrons and the light holes and $s = 4$ for the heavy holes), the tunneling lifetimes are in the range of 100 fs–1 ps.

The tunneling considered here is of the coherent multibarrier type [44]. This requires phase coherence of the wavefunctions for the steady-state resonant probability density to build up in the structure. The tunneling lifetimes therefore have to be smaller than the scattering time since scattering, which includes both elastic and inelastic scattering, would destroy the phase coherence of the wavefunctions. The scattering times can be estimated to a few hundred fs from room temperature measurements of the mobility of the two-dimensional electron gas in modulation doped AlGaAs/GaAs heterostructures [56]. Tunneling from other energy levels than the highest in each well is thus not likely to occur. In the following we therefore consider the intersubband transition of carriers from the lower subbands to the highest by interaction with longitudinal polar optical phonons (LO phonons).

In this analysis we assume that a thermally equilibrated carrier concentration, distributed among the subbands according to Fermi-statistics, is created in the superlattice by absorption of the incident optical pulse. We then calculate the average scattering time for the carriers from the lower to the highest subband. The average intersubband transition rate per carrier from an initial subband n to a final subband m is given by

$$\left\langle \frac{1}{\tau} \right\rangle = \frac{W^-_{\text{tot}} + W^+_{\text{tot}}}{n_n} \tag{20}$$

where τ is the corresponding scattering time, W^-_{tot} and W^+_{tot} are the transition rates due to absorption and emission of a LO phonon, respectively, and n_n is the carrier concentration in subband n. The total transition rates per unit volume are obtained by summation over initial and final states and taking into account the probabilities that the states are occupied and empty, respectively,

$$W^{\mp}_{\text{tot}} = \frac{1}{V} \sum_{\boldsymbol{k}} \sum_{\boldsymbol{k}'} W^{\mp}_{\boldsymbol{k} \to \boldsymbol{k}'} f(\boldsymbol{k})[1 - f(\boldsymbol{k}')] \tag{21}$$

V is the volume of the well and $\boldsymbol{k}$ and $\boldsymbol{k}'$ are the wavevectors for the carrier in the initial state in subband n and in the final state in subband m, respectively. $f(\boldsymbol{k})$ and $f(\boldsymbol{k}')$

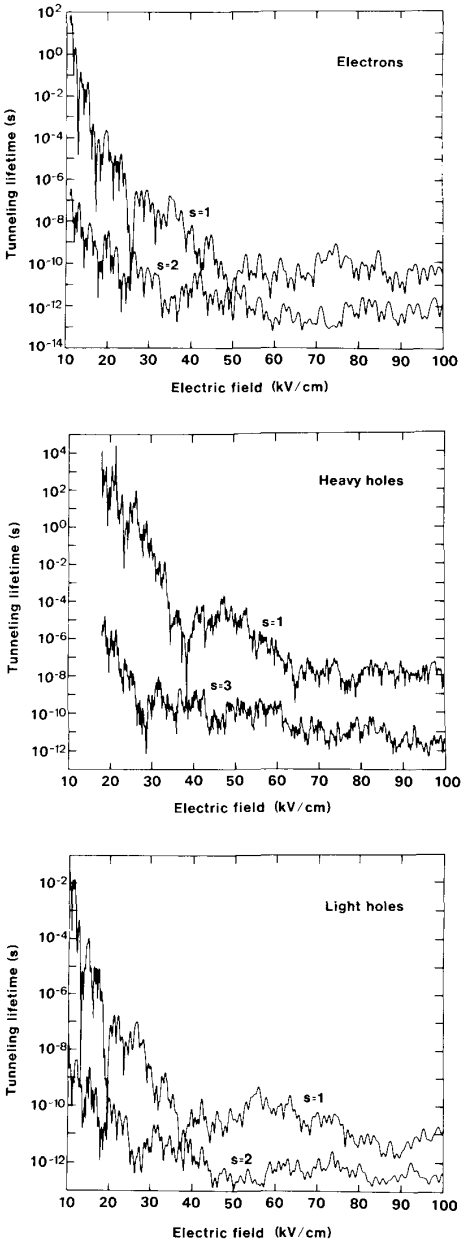

Fig. 8. Tunneling lifetimes for (a) electrons, (b) heavy holes, and (c) light holes confined to different subbands as a function of applied electric field.

are the corresponding occupation probabilities, given by Fermi–Dirac statistics

$$f(\boldsymbol{k}) = \frac{1}{1 + e^{[E(\boldsymbol{k}) - E_F]/kT_c}} \tag{22}$$

where $E(\boldsymbol{k})$ is the corresponding carrier energy, E_F is the carrier quasi-Fermi level, and T_c is the carrier temperature which might differ considerably from the lattice temperature due to the high applied electric field. The transition rate from the initial state $|\boldsymbol{k}>$ to the final state $|\boldsymbol{k}'>$, with corresponding total energies E and E', due to a perturbation H_{ep}, is given by "Fermi's golden rule" obtained by first-order perturbation theory [51]

$$W^{\mp}_{\boldsymbol{k}\to\boldsymbol{k}'} = \frac{2\pi}{\hbar} \left| \langle \boldsymbol{k}' | H_{ep} | \boldsymbol{k} \rangle \right|^2 \delta(E' - E \mp \hbar\omega_0). \tag{23}$$

The delta function expresses the conservation of energy in the scattering process. $\hbar\omega_0$ is the LO phonon energy.

In what follows, our analysis essentially follows that developed by Ridley [57] and Riddoch and Ridley [58]. We assume a bulk phonon spectrum, that is the longitudinal optical phonons are not affected by the presence of the quantum wells and that the carriers can be treated in the effective mass approximation. Screening and Umklapp processes are neglected. We also assume that the LO phonons are dispersionless with an energy equal to that in GaAs (36.5 meV). We approximate the quantum well as a square well with infinite potential barriers at $z = 0$ and $z = L_w$ and neglect the influence of the electric field on the carrier wavefunctions. The wavefunction of the carrier in subband s is then

$$\psi_k(\boldsymbol{r}, z) = \sqrt{\frac{2}{AL_w}}\, u_k(\boldsymbol{r}, z) e^{i\boldsymbol{k}_t \boldsymbol{r}} \sin k_z z \tag{24}$$

where A is the area of the well, $u_k(\boldsymbol{r}, z)$ is the periodic part of the Bloch function, $\boldsymbol{r}$ is the position vector in the xy-plane, $\boldsymbol{k}_t$ is the projection of the carrier wavevector in the xy-plane and k_z, the carrier wavevector in the z-direction, is given by (9). The total carrier energy associated with the state $|\boldsymbol{k}_t, k_z>$ in subband number s is

$$E(\boldsymbol{k}) = E(\boldsymbol{k}_t) + s^2 E_0 \tag{25}$$

where

$$E(\boldsymbol{k}_t) = \frac{\hbar^2 k_t^2}{2m^*} \tag{26}$$

$$E_0 = \frac{\hbar^2}{2m^*} \left(\frac{\pi}{L_w}\right)^2. \tag{27}$$

To account for the finite barrier heights, we use an effective quantum well width L_w such that E_o equals the ground state energy ($s = 1$) calculated from (2) using the true quantum well width. This turned out to be essential, since the energy separation between the subbands, which is sensitive to the quantum well width, affects the intersubband scattering rates. For each electron–phonon scattering process, using the Fröhlich Hamiltonian, the matrix element can be expressed as

$$\left| \langle \boldsymbol{k}' | H_{ep} | \boldsymbol{k} \rangle \right|^2 = \frac{e^2\hbar\omega_0}{2Vq^2} \left(\frac{1}{\epsilon_\infty} - \frac{1}{\epsilon_s}\right) \left(N_q + \frac{1}{2} \mp \frac{1}{2}\right) \cdot \left| G(q_z) \right|^2 \delta(\boldsymbol{k}_t' - \boldsymbol{k}_t \pm \boldsymbol{q}_t) \tag{28}$$

where ϵ_∞ and ϵ_s are the GaAs high frequency and static dielectric constants, respectively, q is the LO phonon wavevector and q_t and q_z its projection in the xy-plane and the z-direction, respectively. The delta function expresses the momentum conservation in the xy-plane and the func-

tion $G(q_z)$ accounts for the uncertainty in the carrier momentum in the z-direction

$$G(q_z) = \frac{2}{L_w} \int_0^{L_w} e^{iq_z z} \sin k'_z z \sin k_z z \, dz. \tag{29}$$

N_q is the Bose–Einstein factor describing the phonon density assuming that the phonons are in equilibrium with a lattice temperature T_L

$$N_q = \frac{1}{e^{\hbar\omega_0/kT_L} - 1}. \tag{30}$$

As shown by Ridley [57], the calculations can be simplified by assuming that the momentum conservation is identical to that in bulk material. This is a good approximation for intersubband scattering. In this so-called momentum conservation approximation the scattering rate from an initial carrier state $|\boldsymbol{k}>$ in subband n to all final carrier states $|\boldsymbol{k}'>$ in subband $m (n \neq m)$ is given by

$$\sum_{\boldsymbol{k}'} W^{\mp}_{\boldsymbol{k}\to\boldsymbol{k}'} = \frac{e^2\omega_0}{8L_w}\left(\frac{1}{\epsilon_\infty} - \frac{1}{\epsilon_s}\right)\left(N_q + \frac{1}{2} \mp \frac{1}{2}\right)$$

$$\cdot \left[\frac{1}{\left[(m-n)^4 E_0^2 + 2(m-n)^2 E_0\left(2E(k_t) \pm \left[\hbar\omega_0 \pm (n^2 - m^2)E_0\right]\right) + \left(\hbar\omega_0 \pm (n^2 - m^2)E_0\right)^2\right]^{1/2}} \right.$$

$$\left. + \frac{1}{\left[(m+n)^4 E_0^2 + 2(m+n)^2 E_0\left(2E(k_t) \pm \left[\hbar\omega_0 \pm (n^2 - m^2)E_0\right]\right) + \left(\hbar\omega_0 \pm (n^2 - m^2)E_0\right)^2\right]^{1/2}} \right]. \tag{31}$$

One example of such a scattering process is illustrated in Fig. 9. Here we show a carrier transition from subband n to subband m by phonon absorption in the momentum conservation approximation. The initial state is in the $k_z = k_n$-plane. As a result of energy conservation, the final state has to be somewhere on the spherical surface indicated by the dashed line. Also, as a result of momentum conservation, the final state is within the $k_z = k'_m$-plane or the $k_z = -k'_m$-plane. This restricts the final state to falling somewhere on the circles indicated in the figure. The summation over the two-dimensional distribution of initial k-states can be replaced by an integration if the number of carrier states in an incremental area in k-space is taken into account

$$\sum_{\boldsymbol{k}} \to \frac{V}{(2\pi)^2 L_w} \int d\boldsymbol{k}. \tag{32}$$

The final expression for the total transition rates is obtained by using polar coordinates in k-space as

$$W^{\mp}_{\text{tot}} = \frac{1}{(2\pi)^2 L_w} \int_0^{2\pi} d\Theta \int_{k_{t\min}}^{\infty} \sum_{\boldsymbol{k}'} \cdot W^{\mp}_{\boldsymbol{k}\to\boldsymbol{k}'} f(\boldsymbol{k})\left[1 - f(\boldsymbol{k}')\right] k_t \, dk_t \tag{33}$$

where the integration over k_t starts at the threshold value

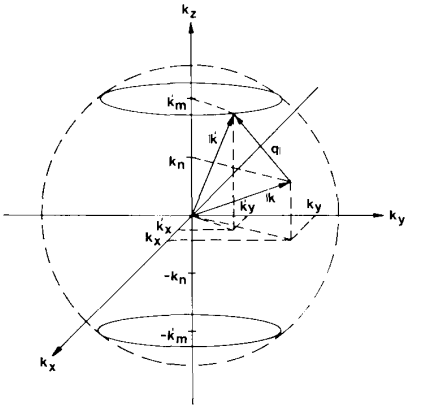

Fig. 9. Illustration in k-space of an intersubband transition by polar optical phonon absorption in the momentum conservation approximation.

$k_{t\min}$ given by

$$k_{t\min} = \sqrt{\frac{2m^*}{\hbar^2}\left[(m^2 - n^2)E_0 \mp \hbar\omega_0\right]}. \tag{34}$$

In the calculations we also need the carrier quasi-Fermi level E_F. This is obtained from the expression for the total carrier concentration in the quantum well, assuming that the carriers are contained in the subbands

$$n_{\text{tot}} = \sum_s \int_{E_s}^{\infty} D(E) f(E) \, dE$$

$$= \frac{m^*}{\pi\hbar^2 L_w} \sum_s \left[E_F - E_s + kT_c \ln\left(1 + e^{(E_s - E_F)/kT_c}\right)\right] \tag{35}$$

where we have used the two-dimensional density of states [5]

$$D(E) = \frac{m^*}{\pi\hbar^2 L_w}. \tag{36}$$

Here we use the true quantum well width and subband energies given by (2), (3). The carrier concentration in

subband s is then given by

$$n_s = \int_{E_s}^{\infty} D(E) f(E)\, dE = \frac{m^*}{\pi \hbar^2 L_w} \left[E_F - E_s + kT_c \ln\left(1 + e^{(E_s - E_F)/kT_c}\right) \right]. \quad (37)$$

The total scattering rates are calculated by numerical integration of (33) and the scattering time is finally given by (20).

The result from such a calculation is shown in Fig. 10. Here we show the average scattering times as a function of carrier temperature from the lower to the highest subband for electrons (e), heavy holes (hh), and light holes (lh) at a lattice temperature of 300 K. By considering the optical pulse power we estimate the total photogenerated carrier concentration to $1 \cdot 10^{17}$ cm^{-3}. At low carrier temperatures (300 K) the scattering times from the ground states ($s = 1$) are the most important, since most of the carriers are confined in these subbands (96 percent of the electrons and 70 percent of the holes). Also the heavy holes are dominant in the valence band since only 10 percent of the holes are light holes due to their smaller effective mass. At higher carrier temperatures, however, more of the carriers are confined in the higher subbands. This is important for the heavy holes in particular, since four confined states exist in the valence band. Due to the smaller scattering times from these states (see Fig. 10) the total effect is a rapid decrease in the average heavy hole scattering time with increasing carrier temperature.

From Fig. 10 we conclude that the scattering times decrease with increasing carrier temperature and are below 10 ps (smallest detectable time constant in the experiment due to the detector circuit bandwidth and the optical pulse FWHM) for carrier temperatures a few hundred degrees above the lattice temperature. This increase in carrier temperature is reasonable to expect at the high electric fields applied perpendicular to the layers. Electric field induced heating of carriers confined in quantum wells have been observed experimentally [59]. These results are consistent with the measured pulse response. At a lower reverse bias voltage, and consequently a smaller applied electric field, a reduced carrier temperature is to be expected. This could explain the observed increase in pulse response FWHM (Fig. 5). The asymmetric pulse response might be due to the different scattering times and therefore different emission times for electrons and heavy holes. The calculated time constant for the thermally assisted tunneling process, being much smaller than the recombination time in the quantum wells, is also consistent with a nearly 100 percent internal quantum efficiency at the operating bias voltage. We believe, however, that our theory slightly underestimates the scattering times since the use of an effective quantum well width, although giving correct ground state energies, gives too large separations between the subbands compared to the exact values as given by (2), (3). Other scattering processes such as acoustic and optical phonon scattering via the deformation potential and carrier-carrier scattering are also neglected. Finally, we believe that the ns-response at the lowest applied field, can be explained by a theory of phonon-assisted transitions from the ground states to the continuum of states above the potential barriers, since at these electric fields, the tunneling lifetimes become very large.

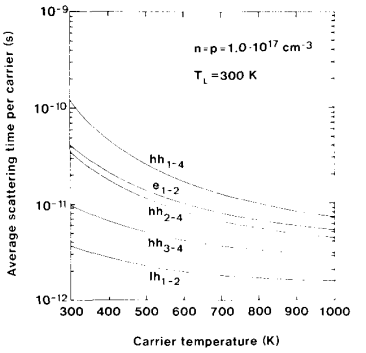

Fig. 10. Average intersubband scattering times due to polar optical phonon interaction for electrons (e), heavy holes (hh), and light holes (lh) from all lower subbands to the highest subband in the quantum well as a function of carrier temperature. The numbers indicate initial and final subband number.

We therefore conclude that a theory of thermally assisted tunneling, taking hot carrier effects into account, is able to predict emission times consistent with the observed bandwidth. Further measurements on the temperature dependence of the temporal response would be valuable to confirm the importance of the phonon interaction.

Also the measurements reported by Collins *et al.* [53] support our theory. Here the carrier transport perpendicular to the layers was found to be thermally activated, decreasing with decreasing lattice temperature. An increase in current conduction was also observed at temperatures below 100 K. This can be explained by an increase in coherent tunneling efficiency from the lower subbands due to a reduced scattering at these temperatures.

The results point out some important design considerations. The choice of high and thick barriers, to enhance the excitonic absorption effects, will slow down the response of the device by increasing the escape times of the photogenerated carriers out of the quantum wells. This could explain the slower pulse response reported by Wood *et al.* [22] in a similar structure ($x = 0.32$ in the barriers), where the slow component is probably due to the thermal emission of heavy holes out of the quantum wells. The choice of low and thin barriers, on the other hand, will result in a fast response but a reduced wavelength selectivity due to reduced excitonic effects. A tradeoff has to be made.

V. Wavelength Demultiplexing

In this section we present results from measurements on the performance of the device as a monolithic wave-

length demultiplexer. Preliminary results have recently been presented [24]. These measurements have been extended here to include a reduced wavelength spacing, an investigation of the polarization dependence of the crosstalk, and bit-error-rate measurements for various crosstalk levels.

The experimental setup for the demultiplexing experiment is shown in Fig. 11. The outputs from two AlGaAs semiconductor lasers operating at 850 (λ_1) and 870 nm (λ_2) were combined in a beam splitter and focused onto the cleaved edge of the demultiplexer using microscope objectives. The spectral positions of these excitation wavelengths are indicated by the dashed lines in the photocurrent spectra shown in Fig. 12. The two detectors were biased at -5 V (V_1) and -15 V (V_2), respectively. With these wavelengths and bias voltages, λ_1 coincides with the heavy hole exciton in the first detector where it experiences a strong absorption. The second wavelength λ_2, however, has a photon energy just below that of the absorption edge of the first detector and will thus be absorbed in the more reverse biased second detector. The lasers were biased at threshold and modulated with 80 ps (FWHM) electrical pulses from step recovery diodes to produce short optical pulses with repetition rates of 500 Mbits/s or 1 Gbit/s. The field from the 850 nm laser was TE-polarized (in the plane of the superlattice layers) while the polarization of the 870 nm laser was either TE or TM (perpendicular to the plane of the layers). The monochromator was used to observe the lasing wavelengths and the longitudinal mode spectra.

Fig. 13 shows the result of the wavelength demultiplexing experiment. The two signals were successfully demultiplexed and detected directly into different electrical channels (u_1 and u_2). However, the residual absorption in detector 1 at 870 nm (see Fig. 12) gives rise to a crosstalk between the channels which is clearly dependent on the polarization. From the experimental data we determine the crosstalk attenuation to be 20 dB for TE polarization and 28 dB for TM polarization.

This dependence on the polarization is a consequence of the anisotropic absorption characteristics in quantum well waveguides [35], as described in Section III-A. For TE polarization the crosstalk is determined by the heavy hole excitonic absorption in detector 1. For TM polarization, however, the heavy hole exciton effectively vanishes and its strength is transferred to the single remaining light hole peak at higher photon energy, thus reducing the crosstalk level, in this case by as much as 8 dB.

The crosstalk depends on the wavelength spacing between the optical signals. It is therefore important to know the acceptable crosstalk level which determines the minimum wavelength spacing. For that reason we have performed bit-error-rate measurements at a data rate of 100 Mbits/s for various crosstalk levels. The experimental setup is shown in Fig. 14. The same lasers (850 and 870 nm) and detector bias voltages as in the preceding experiment were used. A pseudorandom data (PRD) stream at 100 Mbits/s was generated at 850 nm (λ_1). This signal

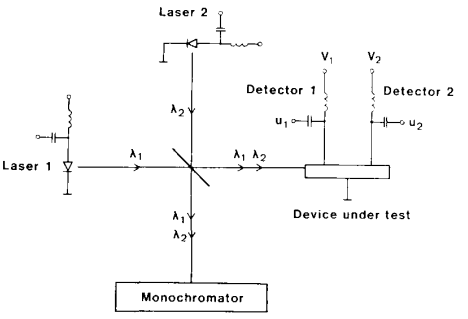

Fig. 11. Experimental setup for the wavelength demultiplexing experiment.

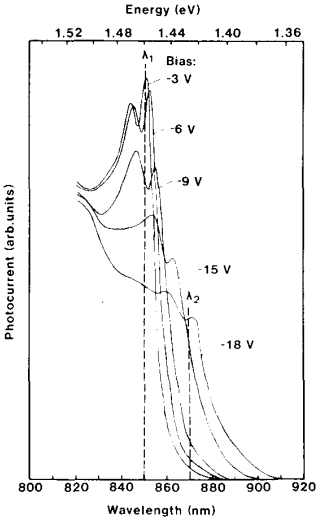

Fig. 12. Photocurrent spectra illustrating the spectral positions of the wavelengths (λ_1 and λ_2) used in the demultiplexing experiment. Detectors 1 and 2 were biased at -5 V and -15 V, respectively.

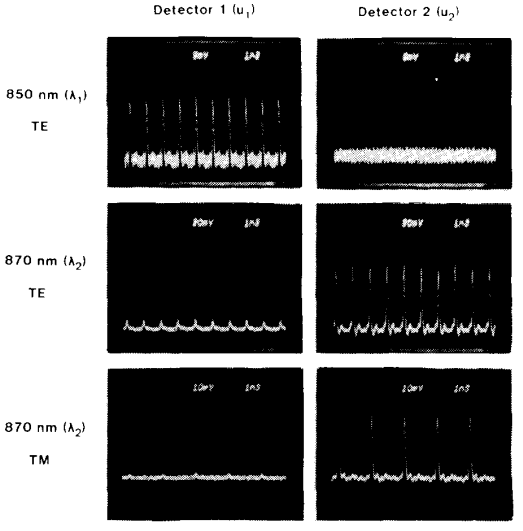

Fig. 13. Results from the dual-wavelength demultiplexing experiment.

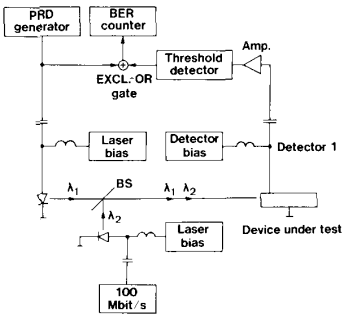

Fig. 14. Experimental setup for bit-error-rate measurements at various crosstalk levels.

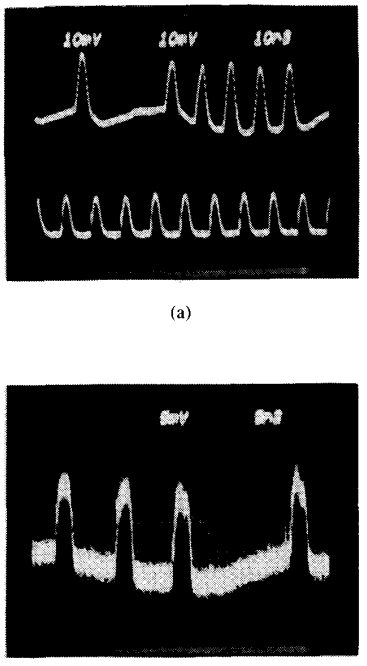

(a)

(b)

Fig. 15. (a) Signals detected by detector 1. Upper trace: Pseudorandom data at 100 Mbits/s and 850 nm. Lower trace: 100 Mbit/s pulse train due to crosstalk from the 870 nm signal. (b) The combined detected signal in detector 1. The sampling oscilloscope was triggered by the data signal.

is shown in the upper trace in Fig. 15(a). The data signal was detected by detector 1, compared to the transmitted data and the bit-errors were counted. Simultaneously, a 100 Mbit/s pulse train was generated at 870 nm [shown in the lower trace in Fig. 15(a)] and combined with the data signal in the beam splitter. This gives a certain crosstalk in detector 1, and different crosstalk levels can be simulated by varying the output power from the 870 nm laser. The combined signal as detected by detector 1 is shown in Fig. 15(b).

The result from the bit-error-rate measurement is shown in Fig. 16. From this we conclude that to achieve a bit-error-rate of less than 10^{-9} a crosstalk attenuation of more than 10 dB is required. This is at least 10 dB below the

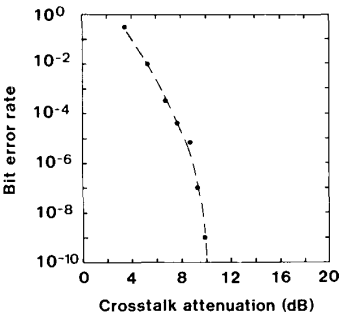

Fig. 16. Bit-error-rates as a function of crosstalk attenuation.

crosstalk attenuations observed in the demultiplexing experiment and indicates that the wavelength spacing could be further reduced while maintaining a satisfactory crosstalk level. It should also be noted that the bit-error-rates recorded here are due to the crosstalk only since the signal levels are far above the noise level.

The results from these experiments and the discussions in Section III indicate that substantial improvements in the demultiplexer performance could be achieved through a number of modifications such as 1) antireflection coating of the cleaved edge, 2) introduction of waveguiding parallel to the layers, 3) increased wavelength selectivity through a more uniform electric field distribution in the superlattice obtained by a reduced impurity concentration, 4) optimization of the lengths of the individual detectors, and 5) the use of dynamic single-mode lasers. We believe that such a device would be able to demultiplex at least three optical channels (by adding more detectors along the waveguide), at a data rate of 5 Gbits/s, with an individual wavelength spacing of 10 nm and a satisfactory degree of crosstalk. An increased responsivity is also expected.

VI. Polarization Sensitive Detection

Finally, we demonstrate the feasibility of using the device as a polarization angle sensor for linearly polarized light. Here we utilize the polarization sensitivity of the absorption characteristics in the quantum well waveguide [35].

The experimental configuration is illustrated schematically in Fig. 17(a). A well-defined linearly polarized excitation was produced by passing the light from the 850 nm laser used in the preceding experiments through a linear polarizer and focusing the beam onto the cleaved edge of the detector using microscopic objectives. The laser was operated continuously well above threshold and placed in an external cavity using a holographic grating for tuning purposes. The polarization of the excitation with respect to the superlattice layers was varied by rotating the detector around the waveguide axis.

Initially, the laser was TE polarized and tuned to 854 nm. Detectors 1 and 2 were biased at -2.5 V (V_1) and -15 V (V_2), respectively. For this polarization the excitation coincides with the low energy side of the heavy

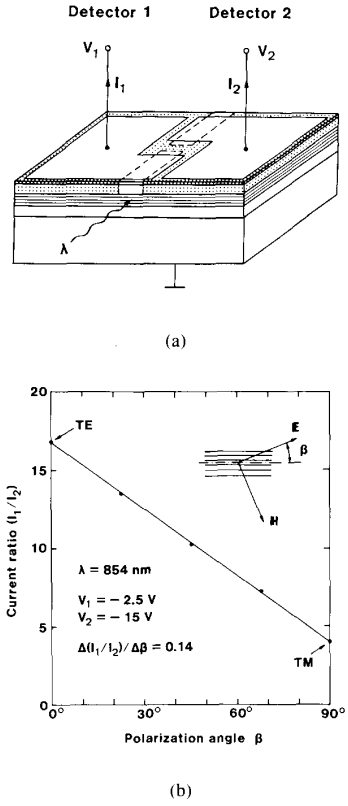

Fig. 17. (a) Schematic view of the device used as a polarization sensor. (b) Current ratio (I_1/I_2) as a function of the polarization angle with respect to the plane of the superlattice layers.

hole exciton in detector 1, thus producing a photocurrent I_1. The length of detector 1 was 7 μm. A photocurrent I_2 was produced by the remaining optical power due to the large reverse bias voltage and the long interaction length (50 μm) in detector 2. When the polarization is continuously changed from TE to TM by rotating the detector, the heavy hole exciton peak gradually loses its strength and more optical power is transmitted through detector 1 without being absorbed, thus decreasing the photocurrent I_1 and increasing the photocurrent I_2. By measuring the ratio I_1/I_2 we obtain a sensitive measure of the polarization angle with respect to the plane of the superlattice layers. This is shown in Fig. 17(b). We also note that by adjusting the excitation wavelength and the detector bias voltages properly, the relation between the current ratio and the polarization angle is highly linear. The gauge factor was determined to be 0.14/degrees under the described conditions. A resolution of a few degrees was easily obtained for the power levels used (about 200 μW of optical power coupled into the waveguide).

The polarization sensor is also expected to be insensitive to the optical power level as long as saturation effects due to the nonlinear excitonic absorption in the quantum wells [8] can be neglected. Also the photocurrents produced have to be larger than the dark currents, which are smaller than 1 nA at the operating bias voltages, corresponding to a lower limit of the optical power of about 1 nW.

VII. Conclusions

The characteristics of voltage tunable SLPD's have been investigated both experimentally and theoretically. The large wavelength selectivity of this device, due to the QCSE, render it attractive for applications such as wavelength demultiplexing. We have developed a theory based on thermally assisted tunneling of photogenerated carriers out of the quantum wells to explain the observed fast temporal response of these detectors.

The performance of a dual-wavelength demultiplexer, consisting of monolithically integrated SLPD's, has been described. The device is capable of demultiplexing two optical signals with a wavelength spacing of 20 nm, a data rate of 1 Gbit/s, and a crosstalk as low as −28 dB. The polarization dependence of the crosstalk as well as its influence on the system performance in terms of bit-error-rate degradation has been investigated. By optimizing the device structure we believe that three optical channels with an interchannel wavelength spacing of 10 nm, operating at more than 5 Gbits/s, can be demultiplexed and detected with a satisfactory degree or crosstalk suppression. Finally, the potential for the device as a polarization angle sensor for linearly polarized light has been demonstrated.

Considering recent advances in epitaxial growth of InGaAsP and InGaAlAs compounds, it is likely that similar devices based on the enhanced electroabsorption effects in superlattices and quantum wells will be developed in these materials [60], [61] for the wavelength region 1.3–1.6 μm which is attractive for fiber optical communication.

Acknowledgment

The authors would like to thank M. Jonsson for helpful discussions.

References

[1] W. T. Tsang, "Molecular beam epitaxy for III-V compound semiconductors," in *Semiconductors and Semimetals, Vol. 22*, W. T. Tsang, Ed. New York: Academic, 1985, part A, ch. 2.

[2] G. B. Stringfellow, "Organometallic vapor-phase epitaxial growth of III-V semiconductors," in *Semiconductors and Semimetals, Vol. 22*, W. T. Tsang, Ed. New York: Academic, 1985, part A, ch. 3.

[3] H. Okamoto, "Semiconductor quantum well structures for optoelectronics—Recent advances and future prospects," *Japan. J. Appl. Phys.*, vol. 26, pp. 315–330, 1987.

[4] R. Dingle, "Confined carrier quantum states in ultrathin semiconductor heterostructures," in *Festkörperprobleme XV*, H. J. Queisser, Ed. Braunschweig: Pergamon Vieweg, 1975, pp. 21–49.

[5] T. Ando, A. B. Fowler, and F. Stern, "Electronic properties of two-dimensional systems," *Rev. Modern Phys.*, vol. 54, pp. 437–672, 1982.

[6] G. Bastard and J. A. Brum, "Electronic states in semiconductor heterostructures," *IEEE J. Quantum Electron.*, vol. QE-22, pp. 1625–1644, 1986.

[7] D. S. Chemla, D. A. B. Miller, P. W. Smith, A. C. Gossard, and W. Wiegmann, "Room temperature excitonic nonlinear absorption and refraction in GaAs/AlGaAs multiple quantum well structures," *IEEE J. Quantum Electron.*, vol. QE-20, pp. 265–275, 1984.

[8] J. S. Weiner, D. S. Chemla, D. A. B. Miller, H. A. Haus, A. C. Gossard, W. Wiegmann, and C. A. Burrus, "Highly anisotropic op-

tical properties of single quantum well waveguides," *Appl. Phys. Lett.*, vol. 47, pp. 664-667, 1985.
[9] D. A. B. Miller, D. S. Chemla, T. C. Damen, A. C. Gossard, W. Wiegmann, T. H. Wood, and C. A. Burrus, "Electric field dependence of optical absorption near the bandgap of quantum well structures," *Phys. Rev. B*, vol. 32, pp. 1043-1060.
[10] Y. Arakawa and A. Yariv, "Quantum well lasers—Gain, spectra, dynamics," *IEEE J. Quantum Electron.*, vol. QE-22, pp. 1887-1899, 1986.
[11] N. Peyghambarian and H. M. Gibbs, "Optical nonlinearity, bistability, and signal processing in semiconductors," *J. Opt. Soc. Amer. B*, vol. 2, pp. 1215-1227, 1985.
[12] J. S. Smith, L. C. Chiu, S. Margalit, A. Yariv, and A. Y. Cho, "A new infrared detector using electron emission from multiple quantum wells," *J. Vac. Sci. Technol. B*, vol. 1, pp. 376-378, 1983.
[13] B. F. Levine, K. K. Choi, C. G. Bethea, J. Walker, and R. J. Malik, "A new 10 μm infrared detector using intersubband absorption in resonant tunneling GaAlAs superlattices," *Appl. Phys. Lett.*, vol. 50, pp. 1092-1094, 1987.
[14] G. Bastard, E. E. Mendez, L. L. Chang, and L. Esaki, "Variational calculations on a quantum well in an electric field," *Phys. Rev. B*, vol. 28, pp. 3241-3245, 1983.
[15] D. A. B. Miller, D. S. Chemla, T. C. Damen, A. C. Gossard, W. Wiegmann, T. H. Wood, and C. A. Burrus, "Band edge electroabsorption in quantum well structures: The quantum confined Stark effect," *Phys. Rev. Lett.*, vol. 53, pp. 2173-2176, 1984.
[16] D. A. B. Miller, J. S. Weiner, and D. S. Chemla, "Electric field dependence of linear optical properties in quantum well structures: Waveguide electroabsorption and sum rules," *IEEE J. Quantum Electron.*, vol. QE-22, pp. 1816-1830, 1986.
[17] T. H. Wood, C. A. Burrus, D. A. B. Miller, D. S. Chemla, T. C. Damen, A. C. Gossard, and W. Wiegmann, "131 ps optical modulation in semiconductor multiple quantum wells (MQW's)," *IEEE J. Quantum Electron.*, vol. QE-21, pp. 117-118, 1985.
[18] T. H. Wood, C. A. Burrus, R. S. Tucker, J. S. Weiner, D. A. B. Miller, D. S. Chemla, T. C. Damen, A. C. Gossard, and W. Wiegmann, "100 ps waveguide multiple quantum well (MQW) optical modulator with 10:1 on/off ratio," *Electron. Lett.*, vol. 21, pp. 693-694, 1985.
[19] D. A. B. Miller, D. S. Chemla, T. C. Damen, T. H. Wood, C. A. Burrus, A. C. Gossard, and W. Wiegmann, "The quantum well self-electrooptic effect device: Optoelectronic bistability and oscillation, and self-linearized modulation," *IEEE J. Quantum Electron.*, vol. QE-21, pp. 1462-1475, 1985.
[20] Y. Arakawa, A. Larsson, J. Paslaski, and A. Yariv, "Active Q-switching in a GaAs/AlGaAs multiquantum well laser with an intracavity monolithic loss modulator," *Appl. Phys. Lett.*, vol. 48, pp. 561-563, 1986.
[21] I. Suematsu, T. Takeoka, M. Yamanishi, and Y. Lee, "Gain-switching characteristics and fast transient response of three-terminal size-effect modulation laser," *IEEE J. Quantum Electron.*, vol. QE-22, pp. 1900-1908, 1986.
[22] T. H. Wood, C. A. Burrus, A. H. Gnauck, J. M. Wiesenfeld, D. A. B. Miller, D. S. Chemla, and T. C. Damen, "Wavelength selective voltage tunable photodetector made from multiple quantum wells," *Appl. Phys. Lett.*, vol. 47, pp. 190-192, 1985.
[23] A. Larsson, A. Yariv, R. Tell, J. Maserjian, and S. T. Eng, "Spectral and temporal characteristics of AlGaAs/GaAs superlattice p-i-n photodetectors," *Appl. Phys. Lett.*, vol. 47, pp. 866-868, 1985.
[24] A. Larsson, P. A. Andrekson, P. Andersson, S. T. Eng, J. Salzman, and A. Yariv, "High speed dual wavelength demultiplexing and detection in a monolithic superlattice p-i-n waveguide detector array," *Appl. Phys. Lett.*, vol. 49, pp. 233-235, 1986.
[25] P. M. Petroff, R. C. Miller, A. C. Gossard, and W. Wiegmann, "Impurity trapping, interface structure, and luminescence of GaAs quantum wells grown by molecular beam epitaxy," *Appl. Phys. Lett.*, vol. 44, pp. 217-219, 1984.
[26] T. Hayakawa, T. Suyamo, M. Kondo, K. Takahashi, S. Yamamoto, S. Yano, and T. Hijikata, "High purity AlGaAs grown by molecular beam epitaxy using a superlattice buffer layer," *J. Appl. Phys.*, vol. 58, pp. 4452-4454, 1985.
[27] S. M. Sze, *Physics of Semiconductor Devices*, 2nd ed. New York: Wiley, 1981, p. 103.
[28] G. Bastard, E. E. Mendez, L. L. Chang, and L. Esaki, "Exciton binding energy in quantum wells," *Phys. Rev. B*, vol. 26, pp. 1974-1979, 1982.
[29] R. C. Miller, D. A. Kleinman, and A. C. Gossard, "Energy gap discontinuities and effective masses for GaAs-$Al_xGa_{1-x}As$ quantum wells," *Phys. Rev. B*, vol. 29, pp. 7085-7087, 1984.
[30] R. L. Greene, K. K. Bajaj, and D. E. Phelps, "Energy levels of Wannier excitons in GaAs-$Ga_{1-x}Al_xAs$ quantum well structures," *Phys. Rev. B*, vol. 29, pp. 1807-1812, 1984.
[31] S. M. Sze, *Physics of Semiconductor Devices*, 2nd ed. New York: Wiley, 1981, p. 77.
[32] R. Dingle, C. Weisbuch, H. L. Störmer, H. Morkoc, and A. Y. Cho, "Characterization of high purity GaAs grown by molecular beam epitaxy," *Appl. Phys. Lett.*, vol. 40, pp. 507-509, 1982.
[33] E. J. Austin and M. Jaros, "Electronic structure of an isolated GaAs-GaAlAs quantum well in a strong electric field," *Phys. Rev. B*, vol. 31, pp. 5569-5572, 1985.
[34] J. A. Brum and G. Bastard, "Electric field induced dissociation of excitons in semiconductor quantum wells," *Phys. Rev. B*, vol. 31, pp. 3893-3898, 1985.
[35] J. S. Weiner, D. A. B. Miller, D. S. Chemla, T. C. Damen, C. A. Burrus, T. H. Wood, A. C. Gossard, and W. Wiegmann, "Strong polarization sensitive electroabsorption in GaAs/AlGaAs quantum well waveguides," *Appl. Phys. Lett.*, vol. 47, pp. 1148-1150, 1985.
[36] H. Iwamura, H. Kobayashi, and H. Okamoto, "Excitonic absorption spectra of GaAs-AlAs superlattice at high temperature," *Japanese J. Appl. Phys.*, vol. 23, pp. L795-L798, 1984.
[37] C. Weisbuch, R. Dingle, A. C. Gossard, and W. Wiegmann, "Optical characterization of interface disorder in GaAs-$Ga_{1-x}Al_xAs$ multiquantum well structures," *Solid State Commun.*, vol. 38, pp. 709-712, 1981.
[38] F. Y. Juang, J. Singh, P. K. Bhattacharya, K. Bajemo, and R. Merlin, "Field dependent linewidths and photoluminescence energies in GaAs-AlGaAs multiquantum well modulators," *Appl. Phys. Lett.*, vol. 48, pp. 1246-1248, 1986.
[39] E. J. Austin and M. Jaros, "Electric field induced shifts and lifetimes in GaAs-GaAlAs quantum wells," *Appl. Phys. Lett.*, vol. 47, pp. 274-276, 1985.
[40] H. Iwamura, T. Saku, H. Kobayashi, and Y. Horikoshi, "Spectrum studies on a GaAs-AlGaAs multiquantum well laser diode grown by molecular beam epitaxy," *J. Appl. Phys.*, vol. 54, pp. 2692-2695, 1983.
[41] A. Alping, R. Tell, and S. T. Eng, "Photodetection properties of semiconductor laser diode detectors," *J. Lightwave Technol.*, vol. LT-4, pp. 1662-1668, 1986.
[42] T. H. Wood, "Direct measurement of the electric field dependent absorption coefficient in GaAs/AlGaAs multiple quantum wells," *Appl. Phys. Lett.*, vol. 48, pp. 1413-1415, 1986.
[43] T. P. Pearsall and M. A. Pollack, "Compound semiconductor photodiodes," in *Semiconductor and Semimetals, Vol. 22*, W. T. Tsang, Ed. New York: Academic, 1985, part D, ch. 2.
[44] F. Capasso, K. Mohammed, and A. Y. Cho, "Resonant tunneling through double barriers, perpendicular quantum transport phenomena in superlattices, and their device applications," *IEEE J. Quantum Electron.*, vol. QE-22, pp. 1853-1868, 1986.
[45] L. Esaki and R. Tsu, "Superlattice and negative differential conductivity in semiconductors," *IBM J. Res. Develop.*, vol. 14, pp. 61-65, 1970.
[46] P. W. A. McIlroy, "Effect of an electric field on electron and hole wavefunctions in a multiquantum well structure," *J. Appl. Phys.*, vol. 59, pp. 3532-3536, 1986.
[47] R. Tsu and G. Döhler, "Hopping conduction in a superlattice," *Phys. Rev. B*, vol. 12, pp. 680-686, 1975.
[48] D. Calecki, J. F. Palmier, and A. Chomette, "Hopping conduction in multiquantum well structures," *J. Phys. C.*, vol. 17, pp. 5017-5030, 1984.
[49] J. F. Palmier, H. Le Person, C. Minot, A. Chomette, A. Regreny, and D. Calecki, "Hopping mobility in semiconductor superlattices," *Superlattices and Microstructures*, vol. 1, pp. 67-72, 1985.
[50] J. F. Ryan, R. A. Taylor, A. J. Turberfield, A. Maciel, J. M. Worlock, A. C. Gossard, and W. Wiegmann, "Time resolved photoluminescence of two dimensional hot carriers in GaAs-AlGaAs heterostructure," *Phys. Rev. Lett.*, vol. 53, pp. 1841-1844, 1984.
[51] B. R. Nag, "Electron transport in compound semiconductors," *Springer Series in Solid State Sciences*, M. Cardona, P. Fulde, and H. J. Queisser, Eds. New York: Springer, 1980, vol. II, ch. 6.
[52] F. Capasso, K. Mohammed, A. Y. Cho, R. Hull, "Effective mass filtering: Giant quantum amplification of the photocurrent in a semiconductor superlattice," *Appl. Phys. Lett.*, vol. 47, pp. 420-422, 1985.
[53] R. T. Collins, K. V. Klitzing, and K. Ploog, "Photoexcited transport

in GaAs/AlAs quantum wells," *Appl. Phys. Lett.*, vol. 49, pp. 406–408, 1986.
[54] R. Tsu and L. Esaki, "Tunneling in a finite superlattice," *Appl. Phys. Lett.*, vol. 22, pp. 562–564, 1973.
[55] G. Bastard, "Superlattice band structure in the envelope function approximation," *Phys. Rev. B*, vol. 24, pp. 5693–5697, 1981.
[56] E. E. Mendez, "Electronic mobility in semiconductor heterostructures," *IEEE J. Quantum Electron.*, vol. QE-22, pp. 1720–1727, 1986.
[57] B. K. Ridley, "The electron-phonon interaction in quasi-two-dimensional semiconductor quantum well structures," *J. Phys. C.*, vol. 15, pp. 5899–5917, 1982.
[58] F. A. Riddoch and B. K. Ridley, "On the scattering of electrons by polar optical phonons in quasi-2D quantum wells," *J. Phys. C.*, vol. 16, pp. 6971–6982, 1983.
[59] R. A. Hopfel, J. Shah, and A. C. Gossard, "Nonequilibrium electron-hole plasma in GaAs quantum wells," *Phys. Rev. Lett.*, vol. 56, pp. 765–768, 1986.
[60] K. Wakita, Y. Kawamura, Y. Yoshikuno, H. Asahi, and S. Uehara, "Anisotropic electroabsorption and optical modulation in InGaAs/InAlAs multiple quantum well structures," *IEEE J. Quantum Electron.*, vol. QE-22, pp. 1831–1836, 1986.
[61] I. Bar-Joseph, C. Klingshirn, D. A. B. Miller, D. S. Chemla, U. Koren, and B. I. Miller, "Quantum confined Stark effect in InGaAs/InP quantum wells grown by organometallic vapor phase epitaxy," *Appl. Phys. Lett.*, vol. 50, pp. 1010–1012, 1987.

Anders Larsson was born in Mariestad, Sweden, on December 5, 1957. He received the M.S. degree in electrical engineering and the Ph.D. degree, both from Chalmers University of Technology, Göteborg, Sweden, in 1982 and 1987, respectively.

From 1984 to 1985 he was with the California Institute of Technology, Pasadena, CA, working with molecular beam epitaxy and optoelectronic quantum well devices under the direction of Prof. A. Yariv. He is currently a Postdoctoral Research Associate at the Research Laboratory of Electro-Optics and Lasers in the Department of Electrical Measurements, Chalmers University of Technology. His current research interests include materials growth by molecular beam epitaxy and the fabrication of optoelectronic quantum well devices for optical communication, integrated optoelectronics, and optical information processing.

Dr. Larsson is a member of the Optical Society of America.

Peter A. Andrekson (S'84) was born in Göteborg, Sweden, on May 31, 1960. In 1984 he received the M.S. degree in electrical engineering from Chalmers University of Technology, Göteborg, Sweden.

In 1984 he joined the Research Laboratory of Electro-Optics and Lasers in the Department of Electrical Measurements, Chalmers University of Technology, where he presently is working towards the Ph.D. degree. His main research interest is the noise and coherence properties of semiconductor lasers and their application to optical communication.

Sverre T. Eng (M'58) received the B.S. degree in electrical engineering in 1952, the M.S. degree in electrical engineering in 1953, and the Ph.D. degree in applied physics in 1967, all from Chalmers University of Technology, Göteborg, Sweden.

From 1953 to 1956 he was engaged in research and development of ultrasensitive microwave receivers for radio astronomy. He later spent ten years at Hughes Research Laboratories, Newport Beach, CA, as a Department Head where he built up a research department in Microwave and Optical Solid State Electronics. He initiated research on parametric diodes, mixers, tunnel diodes, optical detectors, semiconductor lasers, and instrumentation. In 1967 he joined North American Rockwell Corporation, Anaheim, CA, where he spent four years conducting research in lasers and electrooptic systems. Since 1971 he has been Professor and Director of the Institute of Electrical Measurements, Chalmers University of Technology, where he has conducted research in fiber optics communication, applied laser spectroscopy, and optical and digital computer in scientific instrumentation. While on leave from Chalmers University of Technology he has worked as a Consultant and Division Technologist at the Jet Propulsion Laboratory in the area of long range R & D planning, fiber optics, integrated optics, and optical information processing research. He is the author of over 70 technical publications and has several patents.

Dr. Eng is member of the Royal Swedish Academy of Engineering Sciences, APS, and the Optical Society of America.

Amnon Yariv (S'56–M'59–F'70), for a photograph and biography, see p. 72 of the January 1988 issue of this JOURNAL.